Highlights

Earthquake nucleation in the laboratory: insights from space-time imaging of quasi-static precursory slip under tri-axial conditions.

P. Dublanchet, F.X. Passelègue, H. Chauris, A. Gesret, C. Nöel

- We study the nucleation of stick-slip instabilities in a triaxial setup
- Precursory quasi-static fault slip is imaged in space and time from local strain data
- We illustrate a concept of frustrated nucleation leading to macroscopic failure
- Memory effects influence nucleation pattern over repeated fault reactivations

Earthquake nucleation in the laboratory: insights from space-time imaging of quasi-static precursory slip under tri-axial conditions.

P. Dublanchet[a], F.X. Passelègue[b], H. Chauris[a], A. Gesret[a], C. Nöel[b]

[a] *Mines Paris, PSL University, Center for geosciences, Fontainebleau, 77300, France*
[b] *Université Côte d'Azur, CNRS, Observatoire de la Côte d'Azur, IRD, Géoazur, Sophia Antipolis, 06560, France*

Abstract

We study the initiation of frictional instabilities in a saw-cut Westerly granite sample loaded under triaxial conditions reproducing the stress levels at seismogenic depths, up to 90 MPa. By inverting local axial strain measurements, we image the quasi-static (μm.s^{-1}) aseismic slip preceding dynamic slip events in space and time. With this approach we were able to track the expansion of a nucleation zone at about 10-50 m.day^{-1} until the onset of the dynamic rupture that generally occurs when the quasi-static slip fronts reach the boundaries of the experimental fault, suggesting a frustrated nucleation process. We also show that the pre-slip pattern, the expansion rate and the nucleation duration evolve with confining stress and with the successive dynamic reactivation of the fault, that we interpret as a non-recoverable change in the frictional properties in the sample.

Keywords: earthquake nucleation, aseismic slip, critical nucleation length, rupture front, tri-axial loading, saw-cut sample, friction

1. Introduction

Earthquakes could be seen as frictional instabilities developing on critically stressed crustal faults (Ohnaka and Shen, 1999). The initiation, or nucleation of such instabilities, can manifest on real faults as accelerating aseismic slip transients (Roeloffs, 2006; Ruiz et al., 2014; Uchida and Matsuzawa, 2013; Nagao et al., 2014), or foreshock sequences (Dodge et al., 1996; Bouchon et al., 2013; Cabrera et al., 2022). Understanding the physical control on earthquake nucleation is thus key to improve earthquake hazard assessment methods relying on precursors.

The characterization of aseismic nucleation transients on real faults is generally limited by the resolution of geodetic networks, and by the lack of information concerning the state of stress prevailing at seismogenic depths. Earthquake nucleation can instead be studied in the laboratory, by generating stick-slip events on centimetric or metric-scale faults undergoing controlled stressing conditions. A first class of experiments consists of using 2D setups such as direct shear apparatus, allowing to monitor fault reactivation either with local slip sensors distributed along the experimental interface (McLaskey and Kilgore, 2013; Selvadurai and Glaser, 2017), or with photoelasticity techniques when polycarbonate or PMMA material is used as a rock analog (Nielsen et al., 2010; Latour et al., 2013; Guérin-Marthe et al., 2019a; Gvirtzman and Fineberg, 2021). In such metric scale setups, normal stress generally does not exceed 20 MPa. In order to increase the confining stress up to ranges prevailing at seismogenic depths (of the order of 100 MPa for instance), triaxial setups can be used with centimetric scale rock samples (McLaskey and Lockner, 2014; Passelègue et al., 2017; Dresen et al., 2020;

Marty et al., 2023). Under triaxial loading, the approach to stick slip failure can be measured with strain gauge arrays, and acoustic emissions monitoring devices.

Nucleation of stick-slip events revealed by such experiments consists of precursory accelerating aseismic slip (Ohnaka and Shen, 1999; Latour et al., 2013; Dresen et al., 2020), similar to what could be observed for natural earthquakes. Moreover this precursory phase could be associated with intense acoustic emissions interpreted as foreshocks of the main event (Dresen et al., 2020; Marty et al., 2023). Overall, the stick-slip initiation is influenced by the confining stress, the loading rate, the fault roughness (Guérin-Marthe et al., 2019b; Dresen et al., 2020; Guérin-Marthe et al., 2023). Experiments employing a 2D setup with slip sensors or photoelasticity can provide a detailed picture of the spatio-temporal evolution of precursory slip. A first quasi-static stage where slip is localized on a patch that slowly expands along the fault is followed by a transition phase where the slip and expansion (rupture speed) accelerate towards dynamic rupture (Ohnaka and Shen, 1999; Nielsen et al., 2010; Latour et al., 2013; Guérin-Marthe et al., 2019b). Similar techniques however cannot be used in a triaxial setup, so that the spatio-temporal evolution of slip under higher confining stress is less well constrained.

In this framework, we developed recently a kinematic inversion approach to image quasi-static slip along a fault loaded in a triaxial setup relying on strain gauge measurements (Dublanchet et al., 2024). A first application on the nucleation of a stick slip event in granite at 90 MPa confining stress revealed a quasi-static slip event with similar features as the first phase of nucleation observed in 2D setups. The slip event lasted about 20 s, accumulated up to several microns of slip, and expanded at a speed of 100-200 meters per day. Here we extend our preliminary study to a larger data-set: we infer the spatio-temporal evolution of quasi-static slip during the nucleation of 21 stick slip events occurring in Westerly granite, under confining stresses ranging from 30 to 90 MPa.

2. Data and precursory slip imaging

2.1. Data

In the following we analyze the nucleation of 21 among 31 stick-slip events triggered by tri-axial loading of a cylindrical Westerly granite saw cut sample (Figure 1). The experiment is presented in details in Dublanchet et al. (2024). Here we provide a brief summary of the experimental conditions.

The sample is 8.8 cm long and has a diameter of 4 cm. The fault surface, oriented at 30° from the principal stress σ_1, has been polished before loading with a silicon carbide powder (#1200 grit) to approximately achieve a 5 μm roughness. For a given confining pressure $P_c = \sigma_3$, σ_1 is progressively increased by imposing a constant volume injection rate in the axial chamber, until a series of stick slip cycles activates the fault. This procedure is repeated at different levels of increasing (30, 60 and 90 MPa) and decreasing (60 MPa, 30 MPa) confining pressures. The resulting evolution of shear stress along the fault (computed from axial and confining stress measurements) is shown in Figures 1a, b and c. Shear stress drops indicate macroscopic slip events (SE). SEs are initiated at different levels of shear stress, suggesting a change in the effective static friction coefficient f_s across successive fault reactivation (Figure 1d). Overall, f_s tends to remain constant during the increasing confining pressure stages, before increasing from 0.35 to 0.55 during the decreasing pressure stage (Figure 1d). Stress drops during macroscopic slip events furthermore range from 2 to 18 MPa, corresponding to 40-150 μm of coseismic slip (Figure 1e).

Three gap sensors located outside the loading vessel continuously measured the shortening of the whole column (sample and apparatus) during the experiment. This data combined with differential stress measurements is used to estimate the sample shortening, and the average slip occurring on the fault sample, as detailed in Dublanchet et al. (2024). As shown in Figures 1 f, g, and h, slip events are all preceded by micrometric precursory slip accumulation on the fault. This preslip stage is hereafter considered as the nucleation phase.

In addition, an array of 8 strain gauges (G1 to G8) allowed to measure the axial strain ε_{11} at different locations of the sample, and as close to the fault as possible (2.4 mm below it). The position of the gauges is the same as in Dublanchet et al. (2024), and is reported in Figures 2f, S1 to S42 of the supplementary material. In between two SE, the sample experiences both an elastic and an inelastic strain, assumed to result from bulk response and transient fault slip respectively. To extract the inelastic component of strain, we removed the linear trend associated with the elastic response, as detailed in Dublanchet et al. (2024). Examples of resulting inelastic strain arising from nucleation pre-slip is shown in Figure 2a, b and c for increasing confining pressure from 30 to 90 MPa, and in Figure 2d and e for decreasing confining pressure stage.

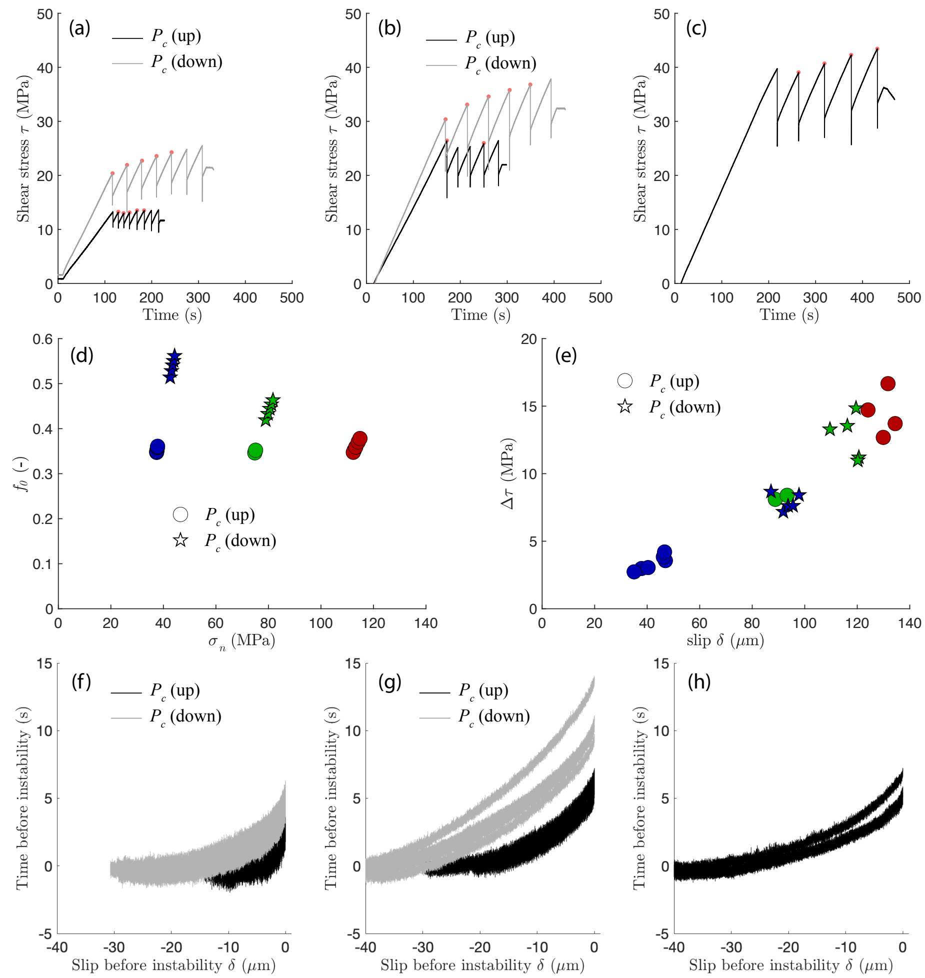

Figure 1: Evolution of the shear stress during stick-slip experiments conducted at 30 (a), 60 (b) and 90 (c) MPa confining pressure. The black curves corresponds to the experiments conducted by increasing the confining pressure from 30 to 90 MPa confining pressure. Grey lines corresponds to the experiments conducted after the one at 90 MPa confining pressure. Red dots indicate the timing of macroscopic slip events (SEs) used in this study. (d) Measurement of the static friction as a function axial normal stress acting on the fault. (e) Evolution of the macroscopic slip as a function of the shear stress drop for each events studied. In (d) and (e), the circles correspond to the events recorded during the increase of the confining pressure. The stars corresponds to the events recorded during the experiments conducted after the experiments at 90 MPa confining pressure, by decreasing the confining pressure to 60 and 30 MPa.(f), (j) and (h). Evolution of the fault slip prior the instabilities during stick-slip experiments conducted at 30 , 60 and 90 MPa confining pressure. The black curves corresponds to the experiments conducted by increasing the confining pressure from 30 to 90 MPa confining pressure. Grey lines corresponds to the experiments conducted after the one at 90 MPa confining pressure.

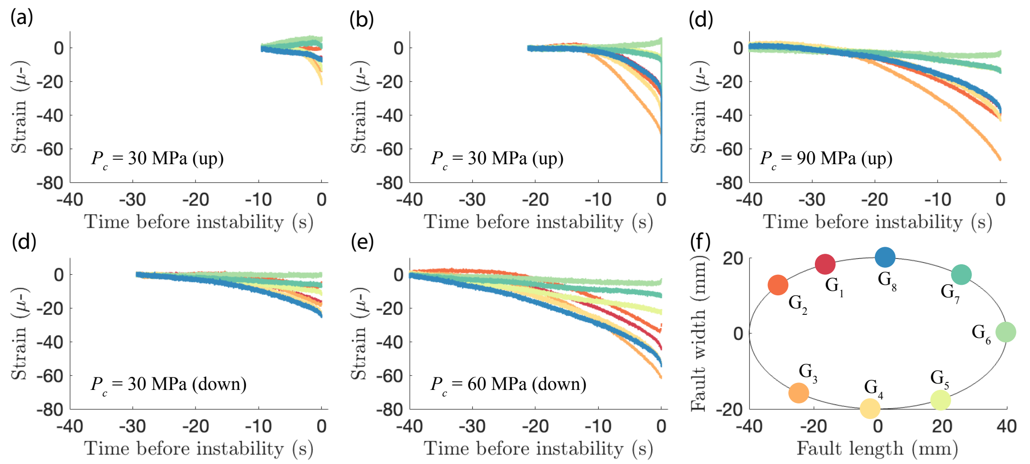

Figure 2: Evolution of axial strain before the instabilites during stick-slip experiments conducted at 30 (a), 60 (b) and 90 (c) MPa confining pressure, and decreasing back the confining pressure to 60 (d) and 30 (e) MPa. One SE per level of confining is shown here. The color lines correspond to the strain gauges location in pannel (f).

2.2. Kinematic inversion of precursory slip

We use the kinematic inversion scheme developed by Dublanchet et al. (2024) to infer from inelastic strain measurements (Figures 2a-e) the spatio-temporal evolution of preslip on the fault during SE nucleation. Here we recall the main features of the method.

The fault surface is discretized using triangular elements, and the fault slip at each node is parametrized as a cosine ramp function of finite duration and amplitude. The inversion scheme allows to retrieve the three parameters (onset time of slip, ramp duration, and slip amplitude) at each node that minimize the squared difference between observed and computed strains at the strain gauge locations, as well as between the observed and computed averaged slip on the fault. In order to compute the strains resulting from a given fault slip distribution, we use a set of elasto-static Green's functions precomputed using a finite elements approach. In doing so, we assume the granite is a homogeneous isotropic elastic medium with Young's modulus E=75 GPa and Poisson ratio ν=0.25 as obtained from the measure of the elastic response of the sample. We also consider the real cylindrical geometry of the sample and the experimental loading as boundary conditions.

For each slip event, we first perform a deterministic optimization step relying on L-BFGS-B algorithm (Broyden, 1970; Fletcher, 1970; Goldfarb, 1970; Shanno, 1970), that converges to a minimum of the cost function (squared difference between modeled and observed strains and slip). Following the synthetic tests presented in Dublanchet et al. (2024), we use at this step a regularization of the cost function aiming at minimizing the gradient norm of the parameters. Based on the synthetic tests of Dublanchet et al. (2024), the regularization parameter we consider here is $\lambda = 0.1$. The resulting best model is used in a second step as an initial model for a global Bayesian exploration carried out with a MCMC algorithm (Metropolis et al., 1953; Hastings, 1970). For each accepted model in the MCMC chain, we reconstruct the slip history of each node, so as to assess the uncertainty on the spatio-temporal evolution of fault slip during nucleation.

The cost function to be minimized during the deterministic optimization and MCMC explorations assumes diagonal covariance matrices, where diagonal elements are computed from the standard deviation of the observed strain and mean slip, i.e. 10^{-6} and $0.1 \mu m$ respectively. These values are readjusted before starting optimization iterations to account for the epistemic uncertainty and for the quality of the strain gauges, estimated by their ability to capture the elastic strain of the sample. All details are provided in Dublanchet et al. (2024).

To ensure convergence of the MCMC, here again we followed the conclusions of Dublanchet et al. (2024), and performed for each SE 10^8 exploration iterations. In general, we achieved an acceptance rate between 0.2 and 0.3. We could however achieve convergence only for 21 of the 31 SE, shown with red dots in Figure 1a, b and c. The 21 SE nevertheless cover the whole range of increasing and decreasing confining pressures.

3. Results

A summary of the space-time evolution of fault slip inferred during the nucleation of 21 SEs is shown in Figure 3. The detailed history of fault slip, and slip-rate are shown in Figures S1 to S43 of the supplementary material. We represent the mean reconstructed slip history, that is the mean prediction of all the models accepted during the MCMC exploration phase. The contours shown in Figure 3 highlight the rupture time t_2: each contour encloses regions of the fault that have experienced more than 2 μm at the time indicated by the colorscale. Note that t_2 is computed from the onset of nucleation: $t_2 = 0$ when the first point of the fault accumulates more than 2 μm of slip. In all of the different cases, nucleation is initiated on a small patch of the fault (hereafter called the nucleation site). The slipping patch then expands in all directions until macroscopic failure (or SE) occurs. For some slip events, we observe a secondary nucleation patch (SE_2 for P_c=30 MPa up, SE_1 for P_c=60 MPa up, SE_1 and SE_3 for P_c=90 MPa up, SE_3 and SE_5 for P_c=60 MPa down, all SE for P_c=30 MPa down). In each case, the

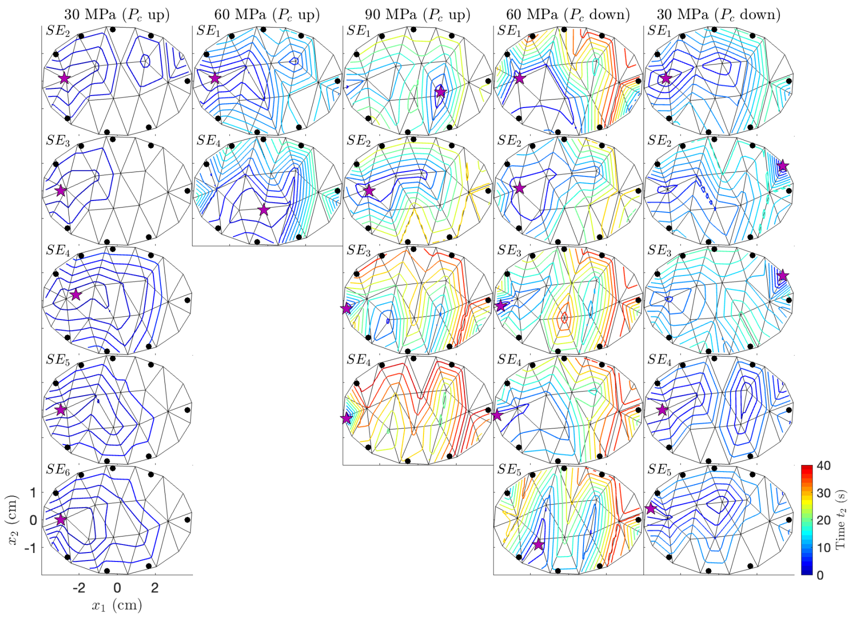

Figure 3: Rupture time t_2, indicating the extent of nucleation patch. Each contour encloses regions of the fault that have experienced more than 2 μm at the time indicated by the colorscale. t_2 is computed from the mean reconstructed slip history. The grid used for the inversion of slip history is shown with solid black lines. Black dots indicate strain gauges position. The magenta star indicates the first node to slip.

total accumulated slip is of the order of 5 to 30 μm, and slip rates range from 0.1 to 5 μm.s^{-1} (Figures Figures S1 to S43). Note that not all nucleation patches reach the fault boundary at the time of macroscopic failure (SE onset), in particular for the first slip events of the ascending confining stage, at P_c=30 MPa. This feature will be further discussed later.

Figure 3 also indicates the nucleation site (star) for the mean reconstructed slip. In order to account for the uncertainty on slip history, we examined how the nucleation sites vary within the whole range of models selected by the MCMC exploration. The results are shown in Figure 4a. Most of the SEs tend to nucleate in the central left part of the fault (close to $x_1 = -2$ cm, $x_2 = 0$ cm), in particular during the increasing confining pressure stages of the experiment (P_c up). The exceptions are SEs triggered at $P_c = 30$ MPa during decreasing confinement that nucleate preferentially on the right part of the fault ($x_1 > 0$). This result could be related to an evolution of the interface properties across repeated failures (SEs) of the fault, as already suggested by the change in effective static friction coefficient shown in Figure 1d. In any case, results in Figure 4a indicate that the nucleation site can hardly be located with a precision smaller than a few centimeters.

In order to better characterize the nucleation of SEs, we next computed the evolution of nucleation patch area S_{nuc} with time to macroscopic failure (SE onset). We defined S_{nuc} at time t as the total area that has accumulated more than u_{th}= 2 μm of slip. We computed $S_{nuc}(t)$ for all the reconstructed slip histories within one standard deviation (1σ) of the average reconstructed slip shown in Figure 3 (and S1 to S43). Recall that the MCMC exploration results in a range of models and thus in a range of slip evolution for each node of the fault. $S_{nuc}(t)$ is represented in Figure 4b and c, for all SEs occurring during the ascending (P_c up) and descending (P_c down) confining pressure stages of the experiment. The rate of surface expansion is also shown in Figure 4d and e.

For all the SEs, the rate of expansion $\dot{S}_{nuc}$ first increases, then decreases when the slip fronts approach the fault boundaries (Figure 4d, e). During the whole nucleation, expansion rates remain below 10^{-3} m^2.s^{-1}. We observe in these Figures that the behavior of the nucleation zone strongly depends

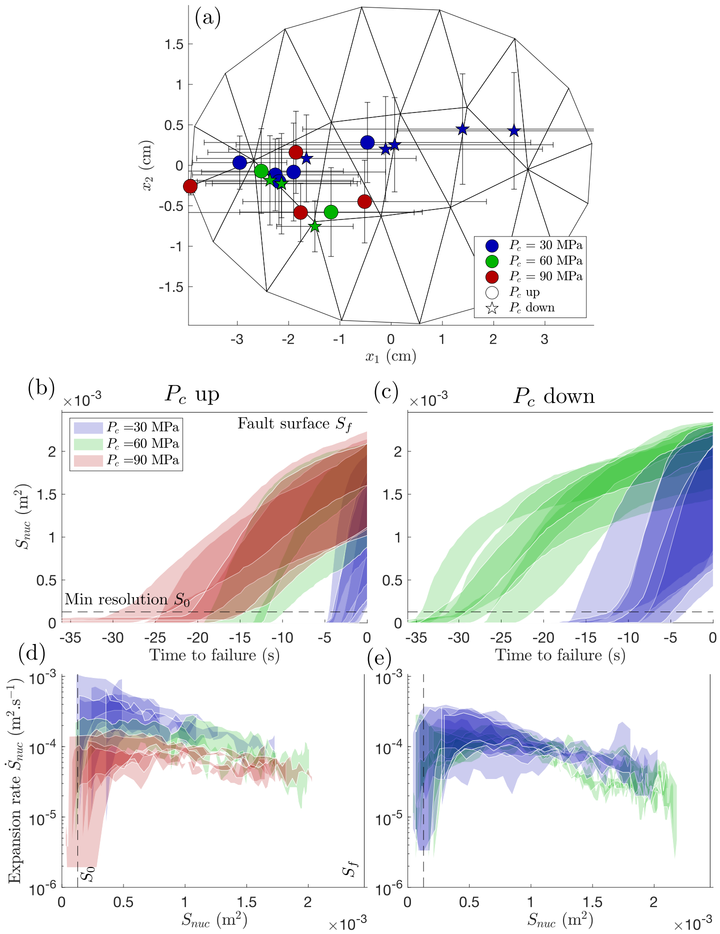

Figure 4: (a): Nucleation site of SE (fault location where slip first exceeds 2 μm). Triangular mesh used for the inversion is shown with thin solid black lines. Symbols indicate the mean nucleation site determined from the reconstructed slip histories of all the models accepted in the MCMC exploration. Error bars indicate the one standard deviation on nucleation site position. (b) and (c): Nucleation zone surface S_{nuc} expansion before macroscopic failure for all the SE occurring during the ascending (a) and descending (b) confining pressure P_c stages of the experiment. The shaded area between two white lines indicates the 1σ range of predictions of the accepted models during the MCMC exploration. The black dashed line indicates the resolution of the inversion method (surface S_0), and the solid black line indicates the total experimental fault surface (surface S_f). (c) and (d): Rate of nucleation zone surface expansion $\dot{S}_{nuc}$ for all the SE occurring during the ascending (c) and descending (d) confining pressure P_c stages of the experiment. Rates are represented as a function of the nucleation zone surface S_{nuc}. Dashed lines indicate the resolution S_0 and total fault surface S_f.

on the confining pressure, and changes with the accumulation of stick slip events on the fault, suggesting again a memory effect.

We report in Figure 5a and b the change in expansion rate $\dot{S}_{nuc}$ and nucleation duration t_n as a function of confining pressure stages. The value of $\dot{S}_{nuc}$ shown here is the average expansion rate before deceleration, that generally occurs when S_{nuc} is larger than $0.3S_f$, S_f being the total available fault surface (Figure 4b and c). t_n is computed as the delay between $S_{nuc} > S_0$ (S_{nuc} larger than the minimum resolution S_0 derived in Dublanchet et al. (2024)) and the onset of the SE.

As the confining pressure increases (P_c up), we observe that the expansion rate decreases (Figure 5a) and the nucleation gets longer (Figure 5c). First events under P_c = 30 MPa nucleate in about 5s, while the same process takes between 12 and 25s increasing P_c from 60 to 90 MPa respectively. Consistently, the expansion rate decreases from $20 - 40$ m^2.day^{-1} to $3 - 5$ m^2.day^{-1}. During the decreasing P_c stages however, the nucleation duration still increases to 30s before decreasing back to about 10s at 30 MPa. The initial duration of 5s is thus not recovered at the end of the experiment. Similarly, the expansion rate slightly increases to $10 - 20$ m^2.day^{-1}, and we do not observe the rapid expansion of the first events under similar confining pressure.

In Figure 5b, we show that the expansion rate $\dot{S}_{nuc}$ approximately scales with the maximum slip rate V_s, except for one event occurring during the decreasing confining pressures stage at P_c=60 MPa. The surface expansion rate $\dot{S}_{nuc}$ of the pre-slip patch can be approximately related to a rupture speed (propagation speed of slip fronts) and the maximum slip rate assuming the pre-slip patch behaves as a circular crack of radius R_{nuc}, so that:

$$\dot{S}_{nuc} = 2\pi R_{nuc}\dot{R}_{nuc} \sim \pi L_f \frac{G}{\Delta\tau_{nuc}} V_s, \qquad (1)$$

where G is the shear modulus of the granite, $L_f = \sqrt{S_f}$ and $\Delta\tau_{nuc}$ the static stress drop driving nucleation. In writing the second equality in equation (1), we used a simple fracture mechanics scaling (Lawn, 1993) to relate the rupture speed $\dot{R}_{nuc}$ and the slip rate V_s. Note that equation (1) is only a rough approximation considering the complex slip pattern shown in Figure 3. As shown in Figure 5b, it nevertheless captures the trend obtained from our inversions, with a stress drop $\Delta\tau_{nuc}$ between 50 and 200 MPa. The outlier corresponds to SE 5 under decreasing confining pressure $P_c = 60$ MPa. As shown in the slip and slip-rate maps of the supplementary material, the inversion has selected models where a single node accumulates all the slip, in a region that is likely poorly resolved. This could explain the small value of expansion rate, and suggests that the MCMC exploration probably did not explore enough the parameter space in this case.

We also compute an effective nucleation length from the surface expansion as:

$$L_c^* = \sqrt{S_{nuc,f}}, \qquad (2)$$

where $S_{nuc,f}$ is the final value of the nucleation patch surface, i.e. at the onset of the SE. The effective nucleation length L_c^* is shown in Figure 5d. The first series of SEs occurring at 30 MPa are characterized by a L_c^* values significantly smaller than the fault length. The nucleation of other SEs consist of a slip event reaching the boundaries of the fault, which manifests

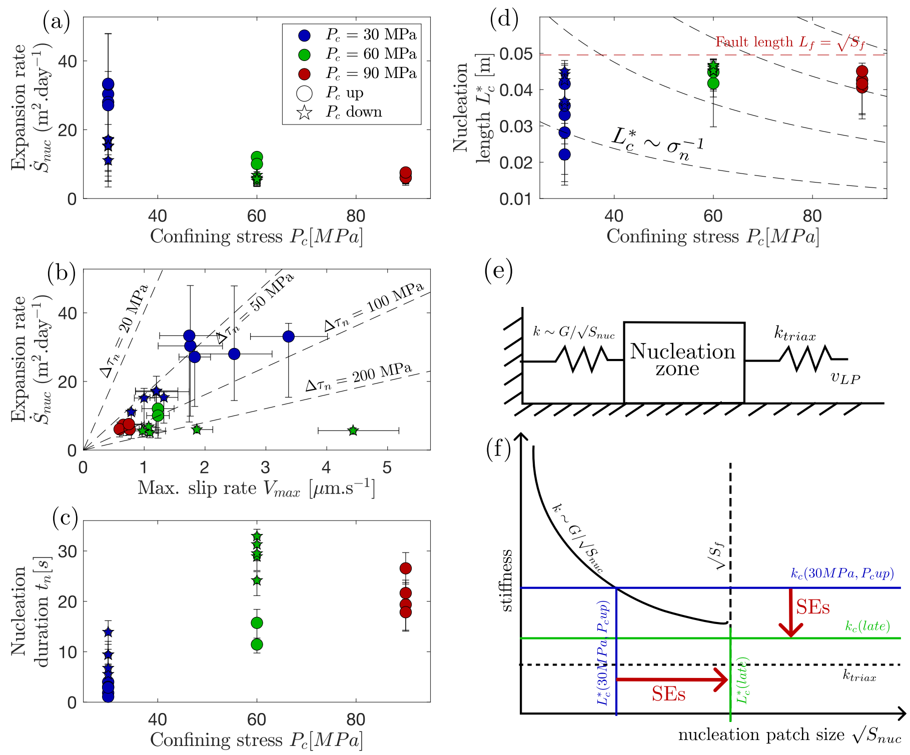

Figure 5: (a) Average rate of expansion of the nucleation zone, computed from results of Figure 4 for $S_0 < S_{nuc} < 0.3S_f$. Error bars indicate the 1σ range of model predictions (shaded areas in Figure 4). (b) Scaling between expansion rate and maximum slip rate on the fault. Dots are inversion results. Black dashed lines indicate the scaling of equation (1) with different values of stress drop $\Delta\tau_{nuc}$.(c) Nucleation duration ($S_{nuc} > S_0$) of SEs. (d) Effective nucleation length L_c^* of SEs. Dots are inversion results. The red dashed line indicates the effective fault length L_f computed as $\sqrt{S_f}$. The black dashed lines indicate theoretical scalings with the inverse normal stress σ_n equation (2). (e): spring-block model of the nucleation zone. v_{LP} corresponds to the shortening imposed by injection in the axial chamber. k_{triax} is the machine stiffness, and k the effective stiffness of the nucleation zone. G is the shear modulus of the rock sample, S_{nuc} the area of the nucleation zone increasing in time as in Figure 4. (e): schematic evolution of stiffness k with nucleation zone expansion, critical stiffness k_c and corresponding nucleation length L_c^* across successive slip events (SEs). k_c and L_c^* evolve towards $k_c(late)$ and $L_c^*(late)$ after the series of SEs.

as L_c^* values close to the fault length, here estimated as $\sqrt{S_f}$. This feature was already shown in Figure 3. Note that even after decreasing the confining pressure back to 30 MPa, the L_c^* remains close to the fault length. We also indicate in Figure 5c the theoretical scaling of the critical nucleation length with inverse normal stress σ_n of the form:

$$L_c^* = \frac{\xi}{\sigma_n} = \frac{Gd_c}{\sigma_n}F. \tag{3}$$

Scaling (3) has been demonstrated for slip-weakening friction (Campillo and Ionescu, 1997; Uenishi and Rice, 2003) and rate-and-state friction (Rubin and Ampuero, 2005) and suggested by previous laboratory experiments (Latour et al., 2013). The factor ξ embeds the shear modulus G, the critical slip d_c for frictional weakening and a functional of other friction parameters F. Under slip-weakening friction, $F = 1/(f_s - f_d)$, where f_s and f_d are the static and dynamic friction coefficients. For rate-and-state friction, F is a function of a (direct effect) and b (state) parameters (Rubin and Ampuero, 2005). Our results indicate that the critical nucleation length does not follow such a simple scaling with constant frictional properties (d_c, f_s, f_d or a and b): as SEs accumulate, L_c^* increases and possibly becomes larger than the experimental fault length. This increase can not be captured by our approach, where L_c^* by definition saturates at $\sqrt{S_f}$.

The occurrence of a SE in cases L_c^* is larger than the fault length instead of stable aseismic slip has to be related to the stiffness of the loading setup k_{triax} (145 GPa.m^{-1} in our case), that remains small enough to allow unstable response. The behavior of the experimental fault could be understood from the simple model illustrated in Figures 5e and f. As long as the nucleation zone (slipping patch) has not reached the fault boundaries, it can be modeled by a spring-block system where a first spring (stiffness k_{triax}) represents the loading due to increasing axial stress, and a second spring (stiffness k) accounts for the stresses related to non-slipping portions of the interface. k is the effective stiffness of the expanding slipping patch, which dimensionally is expected to decrease as $G/\sqrt{S_{nuc}}$ as nucleation proceeds, G being the shear modulus of the rock sample. Note that as long as $S_{nuc} < S_f$, $k >$598 GPa.m^{-1} which is larger than k_{triax}, and the slip evolution is controlled by k in the sense that unstable slip will occur if k becomes smaller than a critical stiffness k_c imposed by normal stress and frictional properties (according to scaling 3, $k_c \sim \sigma_n/Fd_c$). This is what likely happens for the first series of SEs at P_c=30 MPa. If k_c decreases because of interface evolution, k can remain larger than k_c as the nucleation zone grows to the fault boundaries (S_{nuc} reaches S_f). At that point, the model shown in Figure 5(d) does not hold any more, and the rock samples approximately behave as rigid blocks connected to a single spring with stiffness k_{triax}. In other words, k suddenly drops to 0, and the behavior of the fault is only controlled by k_{triax}. SE (or dynamic motion) is then possible if $k_{triax} < k_c$, as illustrated in Figure 5f. The occurrence of SEs is thus possible for a moderate decrease in k_c.

4. Discussion

Using a kinematic inversion method, we were able to image the spatio-temporal evolution of preslip during the nucleation of 21 stick-slip events on the same experimental fault, under 3 different levels of confining pressures P_c. The Bayesian framework used allowed to estimate the corresponding uncertainties, that are essentially related to the gauge network that can only monitor axial strain on the external ream of the fault, as discussed in details by Dublanchet et al. (2024). The mesh used for the inversion is also optimized to get the best resolution while keeping a tractable number of parameters to infer (Dublanchet et al., 2024). Nevertheless our method could reveal a clear evolution of the preslip pattern (preslip duration, expansion rate, final slip, nucleation length) accross successive SEs under increasing then decreasing confining pressure. This evolution is not reversible with respect to changes in confining pressure, suggesting that a non-recoverable mechanical evolution of the interface over successive SEs occurs on top of elastic stress effects. Damage accumulation in the fault zone and wear could translate into roughness evolution and changes in frictional properties.

The increase in L_c^* for instance could be related to a change in the frictional properties of the interface as SEs accumulate on the fault, as suggested by the change in effective static friction f_s shown in Figure 1d. Under rate-and-state friction, the increase in nucleation length could be related to a change in a and b coefficients. Evolution of $a - b$ and d_c with slip has been reported also for quartz rich fault (producing and non-producing gouge) (Scuderi et al., 2017; Noël et al., 2023, 2024). It particularly evolves within the 5 mm of slip, typically what we have here. A similar observation has been done in stick slip experiments involving a bi-material specimen, in particular during the postseismic phase of the main SE (Noël et al., 2025). In any case, the observed change in L_c^* could also indicate an increase of the critical slip d_c throughout the experiment. d_c can increase with normal stress, and thus with confining pressure as observed during dynamic rupture experiments (Paglialunga et al., 2022). However, the increase in d_c reported by Paglialunga et al. (2022) does not exceed a linear scaling, leading to a constant nucleation length with increasing confining pressure according to the scaling of equation (3), and does not explain the non-recovery of L_c^* under decreasing P_c. Because of the uncertainty in our estimated nucleation lengths and on other frictional properties, we cannot rule out alternative modifications of the interface properties.

The nucleation features reported in Figures 3, 4 and 5 were determined using a threshold of 2 μm of cumulative slip, which corresponds to 20 to 50 % of the mean slip accumulated on the fault at the onset of SEs (Figure 1f, g and h). To estimate to what extent the results reported depend on this threshold, we performed the same analysis using a slip threshold of 1 μm. We also considered two cases where the pre-slip zone is defined with a slip-rate threshold of 0.1 and 0.4 μm.s^{-1}. The results are shown in Figures S64 to S72 of the supplementary material. Overall, our conclusions concerning the expansion rates, the nucleation duration, the maximum slip rate, and the memory effect over successive reactivation are not affected by the threshold chosen. Concerning the critical nucleation length however, we still get a non reversible evolution over successive SEs, but the trend strongly depends on the threshold. Using a slip-rate threshold, L_c^* are smaller than when a slip threshold is used. In any case however, many L_c^* values are close to the fault length. Considering the large uncertainty on L_c^* caused by the resolution of the method, but also by the complex shape of the nucleation patch, we could only conclude that L_c^* is of the same order of magnitude than the fault length, so that nucleation process are likely frustrated.

The results presented here (in particular for the critical nucleation length L_c^*) for a series of SEs confirm our previous interpretation (Dublanchet et al., 2024) that with our triaxial setup, we are only able to observe a frustrated nucleation process. We propose here a conceptual model to explain how the experimental fault response is initially controlled by stress interaction along the fault (growth of the nucleation patch), and is suddenly driven by a rigid block response involving the stiffness of the loading device (k_{triax}) when the slip fronts reach the fault boundaries. Note that the rigid block response had already been discussed by Mclaskey and Yamashita (2017). We thus provide here additional evidence to the frustrated nucleation model.

According to the conceptual model of nucleation derived from previous experiments (Ohnaka and Shen, 1999; Nielsen et al., 2010; Latour et al., 2013), we only resolve here the quasi-static stage of nucleation, where expansion rate remains approximately constant, or eventually decreases as the nucleation patch approaches the fault boundaries (Figures 4d and e). Expansion rates $\dot{S}_{nuc}$ ranging from 10 to 50 $m^2.day^{-1}$ as observed would correspond to V_r between 40 and 200 $m.day^{-1}$ according to the simple scaling of equation (1), in the lower range of quasi-static propagation speeds observed during previous nucleation experiments (Latour et al., 2013; Mclaskey and Yamashita, 2017; Selvadurai et al., 2017; Guérin-Marthe et al., 2019b; McLaskey, 2019; Cebry et al., 2022). Similarly, the slip rates involved during pre-slip (between 0.1 and 20 $\mu m.s^1$) typically correspond to the quasi-static range.

Interestingly, we do not capture an acceleration of the expansion towards dynamic rupture, but a slight deceleration of the expansion, which deviates from the classical conceptual model of Ohnaka and Shen (1999); Nielsen et al. (2010); Latour et al. (2013). We suspect this could be a consequence of particular stress conditions related to the small finite size of the fault, or to differences in material (Westerly Granite vs. PMMA) and loading rate, both being features affecting the nucleation process (Guérin-Marthe et al., 2019a). This issue requires further investigation, either with new experiments at a different scale, or using numerical modeling of the fault response.

An important implication of our conclusions regarding the frustrated nucleation concerns the amount of quasi-static aseismic pre-slip moment released by the fault during the nucleation phase. In a perspective of earthquake hazard assessment, it is important to analyze how this quantity scales with the coseimic moment released by the main slip event (SE) (Acosta et al., 2019), the rate of acoustic emissions (Marty et al., 2023) or with material properties and loading. We show here that it can only be accurately estimated in case the nucleation is not frustrated, which requires first characterizing the whole spatio-temporal evolution of slip and the nucleation length.

5. Conclusion

Kinematic inversion of stick-slip events nucleation in a granite saw-cut sample under triaxial conditions reveals how the space-time evolution of quasi-static aseismic slip can change with confining pressure and with the repeated reactivation of the experimental fault. We relate this evolution to a change in frictional properties caused by dynamic slip events of the interface that may dominate over the confining stress effect. Our results illustrate well a frustrated nucleation process on a subcritical fault: an aseismic slip event first grows quasi-statically and instantaneously becomes unstable once it reaches the fault boundaries. The instability is then driven by the loading device stiffness, that remains low enough so that rigid block stick-slip events occur. We thus provide new physical insights into the very early initiation of slip under seismogenic stress conditions, but also propose a new way of interpreting triaxial experiments dedicated to earthquake nucleation.

Open Research

To ensure full reproducibility and ease-of-use of our framework, we provide the data used to perform the inversions at Dublanchet et al. (2025). The MATLAB modules (KISLAB) used for the inversion are accessible at `https://github.com/Pierre-Dublanchet/kislab/releases` Dublanchet (2024).

Acknowledgments

The authors thank C. Twardzik for insightfull discussions about the study. F.X.P acknowledges funding from the European Union (ERC Starting Grant HOPE num. 101041966).

References

Acosta, M., Passelègue, F.X., Schubnel, A., Madariaga, R., Violay, M., 2019. Can precursory moment release scale with earthquake magnitude? a view from the laboratory. Geophysical Research Letters 46, 12927–12937.

Bouchon, M., Durand, V., Marsan, D., Karabulut, H., Schmittbuhl, J., 2013. The long precursory phase of most large interplate earthquakes. Nature geoscience 6, 299–302.

Broyden, C.G., 1970. The convergence of a class of double-rank minimization algorithms: 2. the new algorithm. IMA journal of applied mathematics 6, 222–231.

Cabrera, L., Poli, P., Frank, W.B., 2022. Tracking the spatio-temporal evolution of foreshocks preceding the mw 6.1 2009 l'aquila earthquake. Journal of Geophysical Research: Solid Earth 127, e2021JB023888.

Campillo, M., Ionescu, I.R., 1997. Initiation of antiplane shear instability under slip dependent friction. Journal of Geophysical Research: Solid Earth 102, 20363–20371.

Cebry, S.B.L., Ke, C.Y., Shreedharan, S., Marone, C., Kammer, D.S., McLaskey, G.C., 2022. Creep fronts and complexity in laboratory earthquake sequences illuminate delayed earthquake triggering. Nature communications 13, 6839.

Dodge, D.A., Beroza, G.C., Ellsworth, W., 1996. Detailed observations of california foreshock sequences: Implications for the earthquake initiation process. Journal of Geophysical Research: Solid Earth 101, 22371–22392.

Dresen, G., Kwiatek, G., Goebel, T., Ben-Zion, Y., 2020. Seismic and aseismic preparatory processes before large stick–slip failure. Pure and Applied Geophysics 177, 5741–5760.

Dublanchet, P., 2024. Pierre-dublanchet/kislab: First release. URL: https://doi.org/10.5281/zenodo.13948072, doi:10.5281/zenodo.13948072.

Dublanchet, P., Passelègue, F., Chauris, H., Gesret, A., Twardzik, C., Nöel, C., 2024. Kinematic inversion of aseismic fault slip during the nucleation of laboratory earthquakes. Journal of Geophysical Research: Solid Earth 129, e2024JB028733.

Dublanchet, P., Passelègue, F.X., Chauris, H., Gesret, A., Twardzik, C., Noël, C., 2025. Strain and slip data for kinematic inversion of fault slip during the nucleation of laboratory earthquakes. URL: https://doi.org/10.5281/zenodo.15606648, doi:10.5281/zenodo.15606648.

Fletcher, R., 1970. A new approach to variable metric algorithms. The computer journal 13, 317–322.

Goldfarb, D., 1970. A family of variable-metric methods derived by variational means. Mathematics of computation 24, 23–26.

Guérin-Marthe, S., Kwiatek, G., Wang, L., Bonnelye, A., Martínez-Garzón, P., Dresen, G., 2023. Preparatory slip in laboratory faults: Effects of roughness and load point velocity. Journal of Geophysical Research: Solid Earth 128, e2022JB025511.

Guérin-Marthe, S., Nielsen, S., Bird, R., Giani, S., Di Toro, G., 2019a. Earthquake nucleation size: Evidence of loading rate dependence in laboratory faults. Journal of Geophysical Research: Solid Earth 124, 689–708.

Guérin-Marthe, S., Nielsen, S., Bird, R., Giani, S., Di Toro, G., 2019b. Earthquake nucleation size: Evidence of loading rate dependence in laboratory faults. Journal of Geophysical Research: Solid Earth 124, 689–708.

Gvirtzman, S., Fineberg, J., 2021. Nucleation fronts ignite the interface rupture that initiates frictional motion. Nature Physics 17, 1037–1042.

Hastings, W.K., 1970. Monte carlo sampling methods using markov chains and their applications .

Latour, S., Schubnel, A., Nielsen, S., Madariaga, R., Vinciguerra, S., 2013. Characterization of nucleation during laboratory earthquakes. Geophysical Research Letters 40, 5064–5069.

Lawn, B., 1993. Fracture of brittle solids. Cambridge solid state science series , 307–334.

Marty, S., Schubnel, A., Bhat, H., Aubry, J., Fukuyama, E., Latour, S., Nielsen, S., Madariaga, R., 2023. Nucleation of laboratory earthquakes: Quantitative analysis and scalings. Journal of Geophysical Research: Solid Earth 128, e2022JB026294.

McLaskey, G.C., 2019. Earthquake initiation from laboratory observations and implications for foreshocks. Journal of Geophysical Research: Solid Earth 124, 12882–12904.

McLaskey, G.C., Kilgore, B.D., 2013. Foreshocks during the nucleation of stick-slip instability. Journal of Geophysical Research: Solid Earth 118, 2982–2997.

McLaskey, G.C., Lockner, D.A., 2014. Preslip and cascade processes initiating laboratory stick slip. Journal of Geophysical Research: Solid Earth 119, 6323–6336.

Mclaskey, G.C., Yamashita, F., 2017. Slow and fast ruptures on a laboratory fault controlled by loading characteristics. Journal of Geophysical Research: Solid Earth 122, 3719–3738.

Metropolis, N., Rosenbluth, A.W., Rosenbluth, M.N., Teller, A.H., Teller, E., 1953. Equation of state calculations by fast computing machines. The journal of chemical physics 21, 1087–1092.

Nagao, T., Orihara, Y., Kamogawa, M., 2014. Precursory phenomena possibly related to the 2011 m9. 0 off the pacific coast of tohoku earthquake. Journal of Disaster Research 9, 303–310.

Nielsen, S., Taddeucci, J., Vinciguerra, S., 2010. Experimental observation of stick-slip instability fronts. Geophysical Journal International 180, 697–702.

Noël, C., Giorgetti, C., Collettini, C., Marone, C., 2024. The effect of shear strain and shear localization on fault healing. Geophysical Journal International 236, 1206–1215.

Noël, C., Giorgetti, C., Scuderi, M.M., Collettini, C., Marone, C., 2023. The effect of shear displacement and wear on fault stability: Laboratory constraints. Journal of Geophysical Research: Solid Earth 128, e2022JB026191.

Noël, C., Twardzik, C., Dublanchet, P., Passelègue, F., 2025. On the emergence of fault afterslip during laboratory seismic cycles. Earth and Planetary Science Letters 658, 119288.

Ohnaka, M., Shen, L.f., 1999. Scaling of the shear rupture process from nucleation to dynamic propagation: Implications of geometric irregularity of the rupturing surfaces. Journal of Geophysical Research: Solid Earth 104, 817–844.

Paglialunga, F., Passelègue, F.X., Brantut, N., Barras, F., Lebihain, M., Violay, M., 2022. On the scale dependence in the dynamics of frictional rupture: Constant fracture energy versus size-dependent breakdown work. Earth and Planetary Science Letters 584, 117442.

Passelègue, F.X., Latour, S., Schubnel, A., Nielsen, S., Bhat, H.S., Madariaga, R., 2017. Influence of fault strength on precursory processes during laboratory earthquakes. Fault zone dynamic processes: Evolution of fault properties during seismic rupture , 229–242.

Roeloffs, E.A., 2006. Evidence for aseismic deformation rate changes prior to earthquakes. Annu. Rev. Earth Planet. Sci. 34, 591–627.

Rubin, A.M., Ampuero, J.P., 2005. Earthquake nucleation on (aging) rate and state faults. Journal of Geophysical Research: Solid Earth 110.

Ruiz, S., Metois, M., Fuenzalida, A., Ruiz, J., Leyton, F., Grandin, R., Vigny, C., Madariaga, R., Campos, J., 2014. Intense foreshocks and a slow slip event preceded the 2014 iquique m w 8.1 earthquake. Science 345, 1165–1169.

Scuderi, M.M., Collettini, C., Viti, C., Tinti, E., Marone, C., 2017. Evolution of shear fabric in granular fault gouge from stable sliding to stick slip and implications for fault slip mode. Geology 45, 731–734.

Selvadurai, P., Glaser, S., 2017. Asperity generation and its relationship to seismicity on a planar fault: A laboratory simulation. Geophysical Journal International 208, 1009–1025.

Selvadurai, P.A., Glaser, S.D., Parker, J.M., 2017. On factors controlling precursor slip fronts in the laboratory and their relation to slow slip events in nature. Geophysical Research Letters 44, 2743–2754.

Shanno, D.F., 1970. Conditioning of quasi-newton methods for function minimization. Mathematics of computation 24, 647–656.

Uchida, N., Matsuzawa, T., 2013. Pre-and postseismic slow slip surrounding the 2011 tohoku-oki earthquake rupture. Earth and Planetary Science Letters 374, 81–91.

Uenishi, K., Rice, J.R., 2003. Universal nucleation length for slip-weakening rupture instability under nonuniform fault loading. Journal of Geophysical Research: Solid Earth 108.